Surface-Enhanced Raman and Resonant Rayleigh Scatterings From Adsorbate Saturated Nanoparticles

ARTICLE *in* THE JOURNAL OF PHYSICAL CHEMISTRY C · APRIL 2010

Impact Factor: 4.77 · DOI: 10.1021/jp9093222

4 AUTHORS, INCLUDING:

Li-Lin Tay
National Research Council Canada
62 PUBLICATIONS **1,106** CITATIONS

SEE PROFILE

Surface-Enhanced Raman and Resonant Rayleigh Scatterings from Adsorbate Saturated Nanoparticles

Tay, Li-Lin; Hulse, John; Kennedy, David; Pezacki, John Paul

Publisher's version / Version de l'éditeur:
http://dx.doi.org/10.1021/jp9093222
The journal of physical chemistry. C, Nanomaterials and interfaces, 114, 16, pp. 7356-7363, 2010-03-08

Surface-Enhanced Raman and Resonant Rayleigh Scatterings From Adsorbate Saturated Nanoparticles[†]

Li-Lin Tay,*[,‡] John Hulse,[‡] David Kennedy,[§] and John Paul Pezacki[§]

Institute for Microstructural Sciences and Steacie Institute for Molecular Sciences, National Research Council Canada, Ottawa, Ontario Canada K1A0R6

Received: September 28, 2009; Revised Manuscript Received: February 17, 2010

Collective excitation of conduction electrons in metallic nanoparticles (NP) sustains surface plasmon resonance (SPR) resulting in a large and highly localized amplification of the incident electromagnetic field near the metal NP. This in turn enhances scattered radiation from any molecule in this neighborhood and is the enabling mechanism of surface enhanced Raman scattering (SERS). The optical response of the NPs is highly dependent on their composition, size, shape, and dielectric environment as well as on coupling with nearby particles. In this study, the surfaces of isolated gold NPs and NP dimers, trimers, and multimers were saturated with a Raman reporter molecule (4-(mercaptomethyl)benzonitrile), SERS intensity and surface plasmon resonance profiles were measured, and these were correlated with the nanostructure geometry as revealed by atomic force microscopy (AFM). Dark-field optical microscopy aided in the selection of isolated NPs and was used for measurements of their SPR in the form of resonant Rayleigh scattering spectroscopy. Among all of the probed NPs, all aggregates, including dimers, trimers, and other multimers showed intense SERS activity. All but one of the gold monomers that were examined exhibited no detectable SERS activity. The one exception was an individual triangular nanoprism for which a very weak but detectable SERS signature was observed. We have also calculated the spatial electric field distribution about a spherical monomer, a triangular nanoprism and a dimer of spheres to elucidate the observed differences in their SERS response. The combination of high resolution AFM imaging and light scattering spectroscopies in this study highlights the interdependency of the NP structure, its corresponding SPR response and the role they play in forging strong SERS activity.

Introduction

The localized surface plasmon resonance (LSPR) of a noble metal nanoparticle (NP) manifests itself in a variety of remarkable optical properties with a broad range of applications in sensors, absorbers, imaging, and spectroscopy. Collective excitation of conduction electrons in metallic nanoparticles (NP) sustains surface plasmon resonance resulting in a large and highly localized amplification of both the incident and emission electromagnetic (EM) field near the metal NP, which is largely responsible for surface-enhanced Raman scattering (SERS).[1,2] For small NPs, LSPR behaves like a radiating dipole and contributes to the optical extinction of the NPs that can be monitored by resonant Rayleigh scattering spectroscopy (RRSS) especially in the case of isolated NP.[3] These optical scattering responses (including SERS, RRRS, and extinction) of the NPs are highly dependent on their composition, size, shape, and dielectric environment as well as on coupling with nearby particles. Correlation studies between the nanostructure geometry, LSPR, and SERS response are critical to understanding the nature of this interdependency. This has been explored in part in the single-molecule studies.[4−8]

Single-molecule SERS (SMSERS) studies of colloidal NPs have revealed that intense SERS signal are consistently observed from compact NP aggregates with the simplest aggregate structure being a NP dimer, which is in good agreement with the established theoretical understanding of the coupled LSPR.[8−14] To ensure single molecule-detection, the majority of the SMSERS studies were performed on mildly aggregated colloidal sol incubated with a very low concentration of the Raman reporter molecules (typically a dye molecule). These aggregated colloidal sols are highly heterogeneous with only a very small fraction (<1%) of the NPs (isolated or aggregated) exhibiting SMSERS.[5,8] A consequence of heterogeneity and extreme dilution of the Raman reporter molecule meant a large fraction of the NPs showed no SERS activity. This was likely due either to an absence of adsorbate on the NP or to the adsorbed molecule been positioned too far from the region of highest field enhancement, namely the junctions.

There remain two interesting issues that were not addressed in the SMSERS studies.[4−8] The first is the following: Will any individual NP generate detectable SERS? (In other words, if a single NP is selected at random, will it generate a detectable SERS signal?) The second issue concerns whether all or only specific aggregates can generate detectable SERS activity. To address these issues, we saturated colloidal Au NPs with the nonresonant Raman reporter molecule, 4-(mercaptomethyl)benzonitrile (MMBN).[15] SERS intensity and LSPR profiles were then acquired from various NP species (monomers, dimers, trimers, and multimers) for which the nanostructure could be determined by atomic force microscopy (AFM).

Experimental Methods

Synthesis of The Reporter Molecule. Reagents for the synthesis of 4-(mercaptomethyl)benzonitrile (MMBN) were purchased from Aldrich and used as received. A detailed

[†] Part of the "Martin Moskovits Festschrift".

* To whom correspondence should be addressed. E-mail: lilin.tay@nrc-cnrc.gc.ca. Phone: 613-993-3919.

[‡] Institute for Microstructural Sciences.

[§] Steacie Institute for Molecular Sciences.

10.1021/jp9093222 Published 2010 by the American Chemical Society
Published on Web 03/08/2010

synthesis has been published elsewhere.[15] In brief, 4-(chloromethyl)benzonitrile (1.0 g) was dissolved in H_2O (15 mL) and to this solution thiourea (0.46 g) and NaI (1.0 g) was added. This solution was refluxed for 4 h and then the solvent removed by rotary evaporation. The isolated isothiouronium salt intermediate was then dissolved in dilute aqueous sodium bicarbonate (5 g $NaHCO_3$ in 25 mL H_2O). This solution was refluxed for 2 h and then cooled to room temperature. A white precipitate was collected by vacuum filtration. Thin layer chromatography showed only one band that was determined to be the intended product by mass and ^{1}H NMR spectral analyses.

Preparation of Gold NPs for Imaging. Colloidal Au sol (80 nm) was purchased from Ted Pella. The Au sol was citrate stabilized with a concentration 1.1×10^{10} particles/mL as specified by manufacture. A 25 μL sample of NP is diluted 4-fold by adding 75 μL of deionized (DI) water. To this solution, 4 μL of 0.1 mM MMBN was added. The solution was allowed to incubate overnight. The final sample was prepared by drop casting 1 μL of the incubated sol onto a cleaned microscope coverslip (Fisher Scientific no. 1 glass coverslip) and allowed to air-dry.

Although the precise packing density of MMBN is not known, studies of self-assembled monolayer films on gold surfaces suggest that small head groups such as C≡N (nitrile) typically do not distort the organization of the organic layer nor the sulfur arrangements.[16] Thus, its value would correspond closely to that of the benzenethiol packing density on Au surface which was previously reported[17] as 6.8×10^{14} molecules/cm^2. Using this number as a guide, an 80 nm spherical NP will be saturated by $\sim 1.4 \times 10^5$ molecules. Although AFM and electron microscopy indicate that most of the NPs are slightly larger than the manufactuer's specified nominal size of 80 nm, our experimental conditions provided a sufficient number of MMBN molecules to saturate the surface of the NPs.

Raman Spectroscopy. Raman spectra were acquired with a commercial microRaman system (LabRAM HR, Horiba Jobin Yvon) equipped with a software controlled XYZ stage and a thermoelectrically cooled CCD detector. SERS spectra of NP samples were excited with 632.8 nm radiation at a power density of $\sim 10^3$ W/cm^2. Incident radiation was coupled into an Olympus BX51 optical microscope and focused to ~ 1 μm diameter spot through a 100× objective. The same objective also collects the retro-reflected radiation and guides it to a notch filter that removes the Rayleigh scattered radiation. All SERS Raman spectra were collected with 2 s integration time except for the spectra shown in Figure 3, where the SERS spectra were collected with a 10 s integration time. The Raman spectrum of the MMBN molecule was acquired with a power density of 10^5 W/cm^2 with 4 s integration time. A half-wave plate was inserted in the beam path of the incident radiation for polarization selection. All Raman spectra were presented as raw data without any fitting or background removal.

Resonant Rayleigh Microscopy and Spectroscopy. Resonant Rayleigh images of the NP were obtained in a transmission dark-field microscopy setup adapted to the BX51 Olympus microscope attached to a commercial microRaman spectrometer. The setup is equipped with an oil immersion dark-field condenser (NA = 1.3) and a 100× objective (NA = 0.9). Samples were illuminated with a 75 W xenon lamp and scattered light recorded with a μEye color camera. For spectroscopy, scattered light is directed into the spectrometer dispersed by a 300 groove/mm grating and detected with a CCD detector. All scattering spectra were collected with a 1 s integration time. As the Xe lamp has relatively flat spectral response in the visible region, all scattering spectra in Figures 2−4 are presented as raw data while the normalized scattering spectra are shown in the Supporting Information (Figures S5−6). Background spectrum acquired from a region without NPs (Support Information, Figure S1b) shows the flat spectral response of the Xe lamp.

Atomic Force Microscopy. Atomic force microscopy was performed with a Veeco MultiMode AFM operated in TappingMode. The AFM images were acquired in tapping mode at a horizontal scan rate of 0.5 s/μm. This was achieved with a Si tip on a cantilever with a nominal spring constant of 42 N/m and a nominal resonant frequency of 320 kHz. The orientation of the NPs between AFM and optical microscopy was established through pattern matching by overlaying a low-resolution AFM images to the dark-field optical images.

Discrete Dipole Approximation Calculations. Discrete dipole approximation (DDA) calculations were performed using the DDSCAT codes developed by Draine and Flatau.[18,19] The codes were used without modification. Briefly, the method involves solving for the scattering of an incident electromagnetic wave by a target represented by a simple cubic array of dipoles. The method has been applied with great success to many problems in astrophysics and atmospheric physics and of particular interest for this study it has been successfully applied to light scattering of metallic NPs.[20] Details should be sought in the cited references.

Results and Discussions

We prepared 80 nm Au NPs that were functionalized with the thiol containing Raman reporter MMBN molecule. The particles were then cast dried onto a clean glass coverslip. The lower surface of the coverslip was index-matched to an oil immersion condenser that had been adapted to a commercial Raman microscope as shown in Figure 1a. This provided a direct method to observe both SERS and LSPR response (through resonant Rayleigh scattering spectroscopy) of the isolated NP species. Under dark-field illumination, a number of isolated colored spots were selected and their scattering and SERS spectra were acquired. The sample was then transferred to the AFM and the fine structure of each probed bright spot was imaged at high resolution.

Using dark-field imagery as a guide, one can easily identify isolated NP species. This is illustrated in figure 1b. Four well-resolved bright spots with colors ranged from green to red can be identified. The observed color (spectral response) depends on a number of factors including the shape, geometry as well as coupling (aggregation) of nearby NPs. It is, therefore, necessary to employ high-resolution microscopy techniques to resolve the structural identity of species selected by optical microscopy. In this work, AFM was employed to investigate at high resolution the isolated bright spots on which SERS and RRSS were measured. As an example, the four isolated and diffraction limited spots with green, red, yellow, and orange colors as observed in Figure 1b actually correlate to a spherical monomer (green), a triangular prism (red), an irregularly shaped spheroid (yellow), and a closely spaced trimer and monomer that showed up as a single diffraction limited spot of orange color as shown in Figure 1c.

The small Raman active molecule used in this study, MMBN, contains a methyl thiol and a terminal nitrile in an ortho−para-substituted benzene ring as shown in the chemical structure in Figure 1d. This species was designed specifically as a "Raman reporter" molecule for tracking NP by SERS. There are a few reasons for this choice. First of all, MMBN is a robust molecule with a relatively simple spectroscopic signature. Second, it is

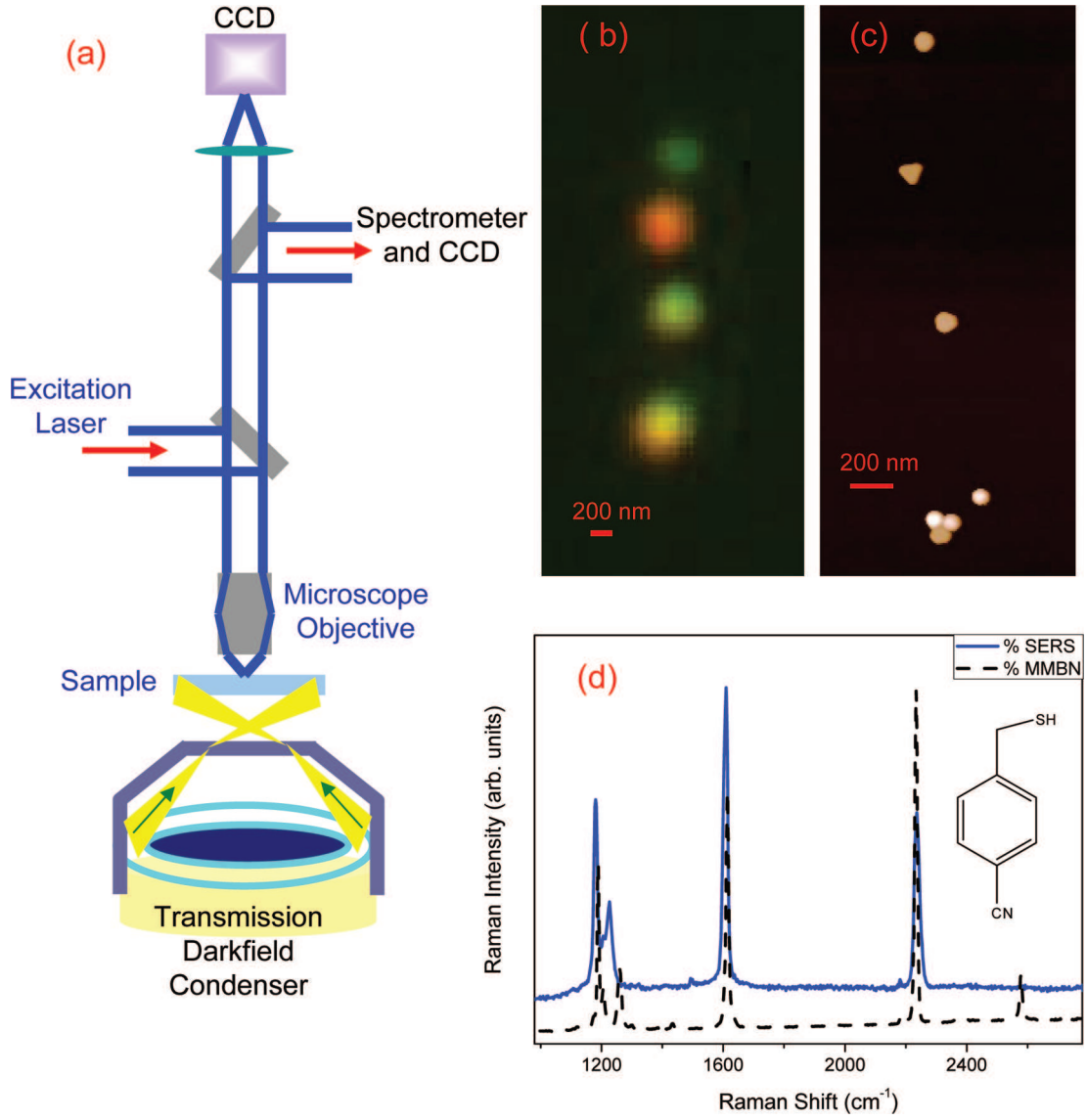

Figure 1. (a). A dark-field condenser adapted to a commercial microRaman spectrometer to enable both Rayleigh and SERS spectroscopy. (b) Four isolated Rayleigh scattering spots as viewed under darkfield illumination. (c) Atomic force microscopy image of the same area revealed the NP structure responsible for the four colored spots in (b). Note that the lowest spot in (b) comprised two sets of closely spaced NPs, a trimer and a monomer, that were not resolved by optical microscopy. (d) Dashed and solid traces are the Raman and SERS spectrum of the MMBN Raman reporter molecule. The chemical structure of MMBN is shown as an inset.

advantageous to avoid possible photodegradation during the measurements by using a molecule that is not in resonance with the excitation radiation (632.8 nm in the present case). This will allow for greater experimental flexibility, for example, excitation with higher power. Lastly, increasing use of the MMBN molecule in SERS imaging applications in our other recent work prompted us to fully characterize its SERS behavior in this correlation study.[15] MMBN can be coordinated onto an Au surface through the terminal thiol moiety. Its attachment to Au also reduces the repulsive surface charge resulting in the mild aggregation of colloidal sols that is necessary for sustaining a strong SERS response. A typical Raman spectrum of the MMBN powder (shown as the dashed trace in Figure 1d) is dominated by three features. A doublet at 1180 and 1226 cm^{-1} is from a symmetric in-plane aromatic ring C−H mode while the two strong sharp bands at 1609 and 2220 cm^{-1} are from a symmetric in-plane aromatic ring deformation and the nitrile C≡N stretch, respectively. A weaker band at 2600 cm^{-1} from the thiol S−H stretch is also observable. A bulk SERS spectrum of the MMBN molecule (obtained from a very large aggregate of Au NPs) is shown as the solid blue trace in Figure 1d. The SERS spectrum closely resembles the powder spectrum with two notable differences, the lack the of S−H stretch and an inversion in the intensity ratio of the 1609 cm^{-1} and 2220 cm^{-1} bands (1:2 in the powder, 2:1 in SERS spectrum). The loss of the S−H vibration can be used as an indicator of successful conjugation of the MMBN molecule onto Au surface.

Figure 2 shows correlated dark-field image, AFM images, resonant Rayleigh scattering spectra, and SERS spectra of three monomer particles. The particles have been labeled as I, II, and III for easy reference. NP I has a faint green color under dark-field illumination and an asymmetric Rayleigh scattering spectrum peaked at 550 nm with a full width at half-maximum (FWHM) of 74 nm. AFM analysis revealed that this green spot corresponds to a sphereoid NP with an approximate diameter of 80 nm. (Figure S2 Supporting Information) This spectral feature is red-shifted and somewhat broader than the 515 nm peak (with FWHM 60 nm) of the scattering spectrum calculated by DDA for an 80 nm Au sphere in vacuum (Figure S4, Supporting Information). The presence of the MMBN molecule

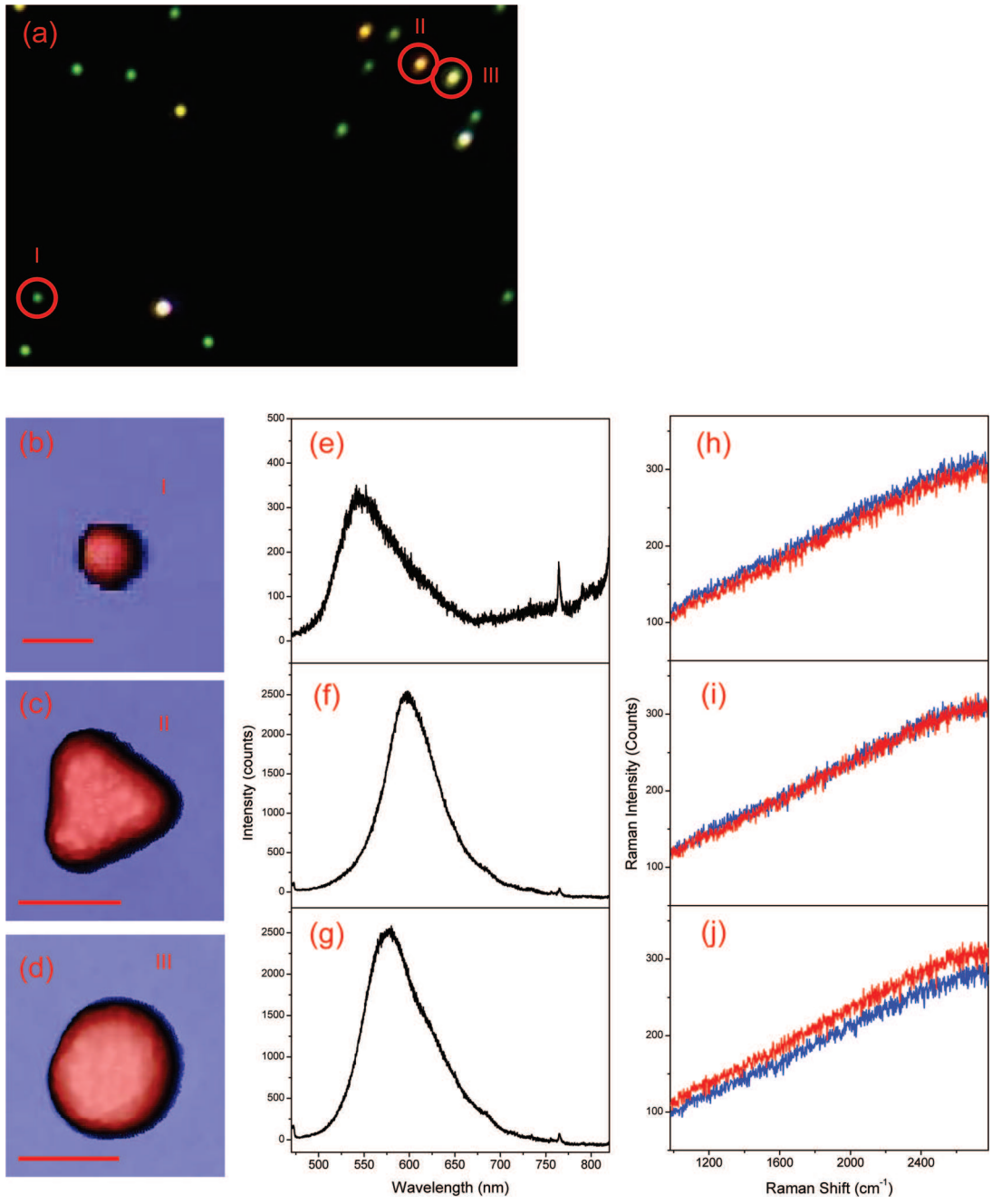

Figure 2. A correlated view of a dark-field optical image, AFM images, Rayleigh scattering, and SERS response for three monomer NPs. (a) Dark-field illumination of a dispersed region where three selected spots (circled and labeled I, II, and III) were probed. (b,e,h) AFM image, Rayleigh scattering, and SERS response, respectively, of particle I, a spherical NP. (c,f,i) AFM, Rayleigh, and SERS response, respectively, of the triangular nanoprism, II. (d,g,j) AFM, Rayleigh, and SERS response of the particle III, a lozenge NP. For the SERS spectra (h−j), the polarization of the incident light is indicated by trace color, blue for vertical and red for horizontal. The scale bars are 100 nm.

on the Au NP surface and its proximity to a substrate (glass) with a refractive index greater than vacuum can both cause a red shift in the measured scattering spectra. The broadening of the experimentally observed scattering spectrum is likely a result of deviation of the NP shape from a perfect sphere. The orange and yellow colored particles II and III have resonant Rayleigh scattering responses that are approximately 10× greater than for the spherical NP I. The AFM image of II is a triangular prism with rounded corners and an altitude of 117 nm and a thickness of approximately 60 nm. This NP has a much more symmetric LSPR response centered at 600 nm with FWHM 67 nm. The DDA calculated scattering response of an equilateral triangular nanoprism with side 118 nm and thickness 60 nm has a scattering response peaked at 660 nm. The shorter wavelength peak position observed experimentally is likely due to differences between the ideal prism used in the calculation and the actual geometry of the measured NP. Kelly et al. have shown in a similar DDA calculation that truncating or "snipping off" of the sharp corner of the nanoprism, leads to a substantial blue shift in the extinction spectrum of a silver nanoprism.[20] The AFM profile of NP III revealed an oval-shaped-disk with axes of length 123 and 131 nm and height of 60 nm. This particle has a broad LSPR centered at 575 nm with a FWHM of 81 nm. Probing the SERS activity with 632.8 nm excitation radiation and a power density of 10^3 W/cm^2 yielded no observable SERS activities from these individual NPs (as shown in Figure 2h−j). Taking advantage of the robustness of the MMBN molecule and its nonresonant nature with the exciting

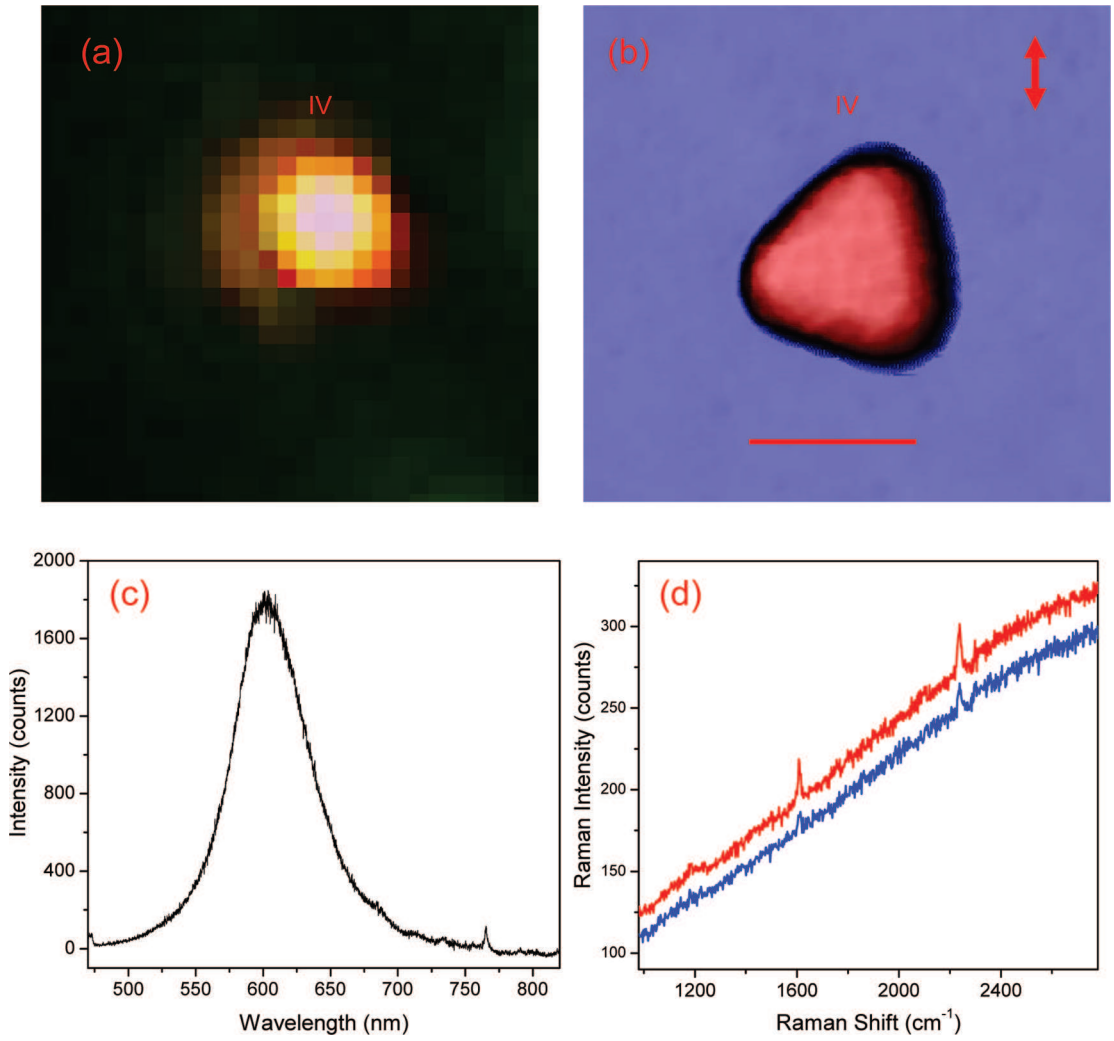

Figure 3. Correlation of dark-field optical image (a), AFM image (b), Rayleigh scattering (c), and SERS response (d) of a triangular nanoprism labeled as particle IV. The blue trace in (d) was obtained from incident radiation polarized in the vertical direction whereas the red trace was for incident radiation polarized in the horizontal direction. The scale bars are 100 nm.

radiation, we also probed these NP monomers with an increased power density (10^4 W/cm^2). Even at the elevated excitation power, no SERS activity was observed from these NP monomers. Although this observation is consistent with the reported SMSERS studies, we note that the Au NPs employed in this study were intentionally saturated with the reporter molecules. There is another noteworthy point. Although the triangular prism II exhibited an LSPR response peaked very close to the wavelength of the Raman excitation radiation and so presumably was optimized for SERS, no SERS activity was observed.

In a typical experiment, AFM showed that about 60% of the probed spots were single NP (monomer). With the exception of a single triangular shaped nanoprism (Figure 3, labeled as particle IV), none of these monomer NPs exhibited observable SERS activity. Figure 3a shows the single orange-redish dark-field scattering spot that is the light scattered by particle IV. The AFM image of IV (Figure 3b) shows the triangular nanoprism with rounded edges. This triangular prism has an altitude of 117 nm and height of 52 nm. The LSPR scattering response of IV has a symmetric peak centered at 600 nm with fwhm of 66 nm. IV closely resembles the nanoprism monomer II of Figure 2c. Both have similar size, shape (both with rounded edges) and LSPR scattering profiles. But the two differ markedly in their SERS response. While II showed no SERS response, IV has weak but observable SERS activity as shown in Figure 3d. The blue SERS spectrum in Figure 3d was obtained from the vertically polarized excitation radiation while the red trace from the horizontally polarized light. Integration of the band intensity of the nitrile vibrational mode showed that the SERS response from the horizontally polarized excitation radiation is approximately 50% higher than the SERS spectrum from the vertically polarized excitation.

To deepen our understanding of the enhancement factor differences between the various individual NPs and NP aggregates we performed DDA calculations of scattering spectra and electric field distributions for these systems. The electric field distributions presented below were calculated for excitation at 635 nm. Figure 5 shows the electric field spatial distributions as false color maps of |E| for a spherical NP (Figure 5a), a triangular nanoparism (Figure 5b,c) and a dimer of spheres touching (Figure 5d) and separated by one nm (Figure 5e,f).

Figure 5a shows a false color electric field distribution calculated for an 80 nm Au sphere bathed in incident radiation of unit field amplitude with the electric field oriented vertically. (With the incident electric field component written as $E_0\, e^{-i\omega t}$, the resultant electric field strength is expressed in units of E_0.) The maximum electric field was found to be 7 at positions just outside the sphere at its extremities along an axis codirectional with the direction of the incident polarization. Figure 5b,c shows false color electric field maps calculated for a triangular

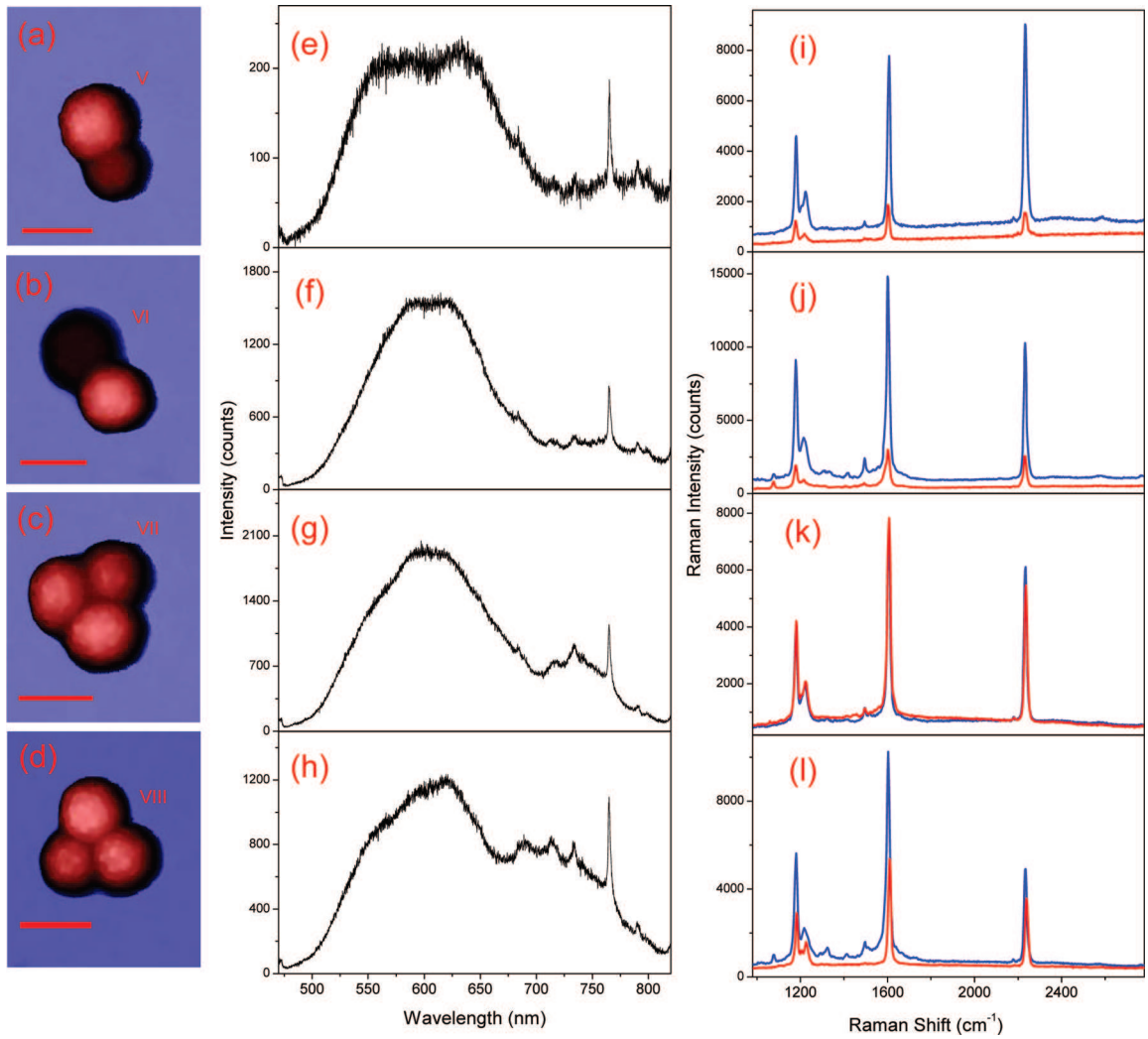

Figure 4. Correlation of AFM, Rayleigh scattering, and SERS response from aggregated NPs. (a,e,i) AFM image, Rayleigh scattering spectrum, and SERS response of a spherical dimer, V. (b,f,j) AFM image, Rayleigh scattering, and SERS response of a disk−sphere dimer, VI. (c,g,k) AFM image, Rayleigh scattering, and SERS response of a trimer aggregates, VII. (d,h,l) AFM image, Rayleigh scattering, and SERS response of trimer aggregates, VIII. The scale bars are 100 nm.

nanoprism, albeit with sharp corners but otherwise similar to the NP IV discussed above. The calculation was performed with the electric field oriented ∼22 and 112° to the vertical bisector of the equilateral triangle. This mimics the angular orientation of the experimentally observed triangular nanoparism IV (Figure 3b). We estimated enhancement factor difference between the two excitation polarizations to be 25%. This number was determined by integrating the enhancement factor over the entire nanoprism. The figures show that the regions of highest electric field are located at the three corners of the nanoprism. The maximum electric field of 78 leads to an approximate SERS enhancement of $\sim 10^7$ based on the $|E|^4$ dependency. This provides a rough estimate of 4 order of magnitude difference in the SERS enhancement factor for the triangular nanoparism over the 80 nm spherical NP. Such large deviation would certainly explain that no SERS activity was observed form the spherical particles. Although the maximum electric field in Figure 5b is somewhat higher than in Figure 5c, one does anticipate the overall enhancement to be higher in Figure 5c when the extra field contribution over the proper collection solid angle and the fact that both corners at the base of the nanoprism benefit from the field oriented at 112° are taken into consideration. This agrees with the experimentally observed SERS signatures, with the horizontally polarized SERS showing slightly higher integrated intensity.

The fact that weak SERS activity was observed from IV but not from II shows the "hot-site" dominant response of SERS. The overall LSPR response of the nanostructure provides a measure of the total integrated field energy density around the nanoprism but carries no information about the spatial distribution of the local field which is highly dependent on the local structural variations of the nanostructures.[3] Hence, in this case, although both triangular nanoprisms showed very similar LSPR response, very different SERS response was observed. The DDA calculations of Schatz et al. have demonstrated that slight variation at the corners of the nanoprism results in notable difference in the LSPR response, particularly in the local field maxima.[21] It is entirely possible that although the LSPR responses of both prisms are similar, the local fields responsible for producing the strongest SERS are different, resulting in the observed SERS activity. Another (perhaps less plausible) explanation would be that no reporter molecule was present at the sites with the most intense fields in the case of the nanoprisms II, so that although molecules covered other portions of the NP, they could not benefit from the high field intensity at the localized "hot-sites" of the NP. This is an important

observation in demonstrating that the SERS activity from a single NP is detectable.

Figure 4 shows the correlation of AFM images (a−d), LSPR (e−h), and SERS (i−l) responses of four NP aggregates (labeled as particles V−VIII). Their corresponding dark-field image is shown in the Supporting Information (Figure S1a). V and VI show two slightly different NP dimers with complex and broad LSPR responses (Figure 4e,f) covering almost the entire visible region from 500 to 700 nm. The dimer V is made up of two slightly different sized NPs with diameters 106 and 91 nm as suggested by the AFM profile in the Supporting Information (Figure S3a,b). The interparticle axis is oriented at approximately 13° to the vertical direction. The dimer VI consists of a disklike NP (diameters 118 nm and height 50 nm) and a spherical NP. (Supporting Information, Figure S3c-d) The interpartical axis of this disk−sphere dimer is oriented at approximately 34° to the vertical direction. The scattering response of the disk−sphere dimer (VI) is approximately 1 order of magnitude larger as compared to the sphere−sphere dimer (V). Both dimers exhibit intense SERS activities with strong excitation polarization dependencies as shown in their SERS spectra in Figure 4i,j. The blue spectra were obtained from the vertically polarized excitation and the red spectra from the horizontally polarized radiation. The polarization dependency (polarization anisotropy) of these dimer echoes the observation in the SMSERS studies.[12,22] Theoretical calculations and experimental observation from the SMSERS studies had revealed that the strongest SERS intensity is observed when the dimers are excited with light polarized parallel to the interparticle axis. On the contrary, SERS intensity diminishes when the polarization becomes perpendicular to the interparticle axis. The interparticle axes of both dimers V and VI are oriented sufficiently close to the vertically direction that they may be considered to be oriented near parallel to the plane of polarization for vertically polarized Raman excitation. This then explains the strong SERS signal in this case. In the SMSERS studies, the SERS intensity is extremely small (typically not observable) when excited with light perpendicular to the interparticle axis. As the horizontally polarized radiation is not exactly perpendicular to the interparticle axis of the dimers probed in this study, we did observe a smaller but noticeable SERS response from the horizontally polarized excitation. SERS intensities for the vertically polarized radiation are approximately 5 times stronger than for the horizontally polarized radiation in both dimers.

DDA calculations were also performed for the case of two 80 nm Au spheres in close proximity. Figure 5d−f shows false color electric field maps for these cases. The maps are cross sections along the interparticle axis. The maximum electric field strength about tightly coupled dimer NPs is located in the neighborhood of the interparticle junction and this maximum electric field strength depends strongly on the particle separation as is shown in Figure 5d−f. The maximum field strength calculated for a touching dimer is approximately 55 times higher than for a spherical NP and 6 times higher than a triangular nanoprism. This implies a SERS enhancement of approximately 7 orders of magnitude for the spherical dimers over the spherical NP (monomer) and 3 orders of magnitude enhancement over the triangular nanoprism. Figure 5f shows the electric field distribution when the electromagnetic field incident on the dimer is polarized perpendicular to the interparticle axis. In this case, the electric field distribution resembles that of two isolated NPs with the regions of maximum electric fields located at the extremities of the two NPs along the axis codirectional with the direction of the incident polarization. It should also be

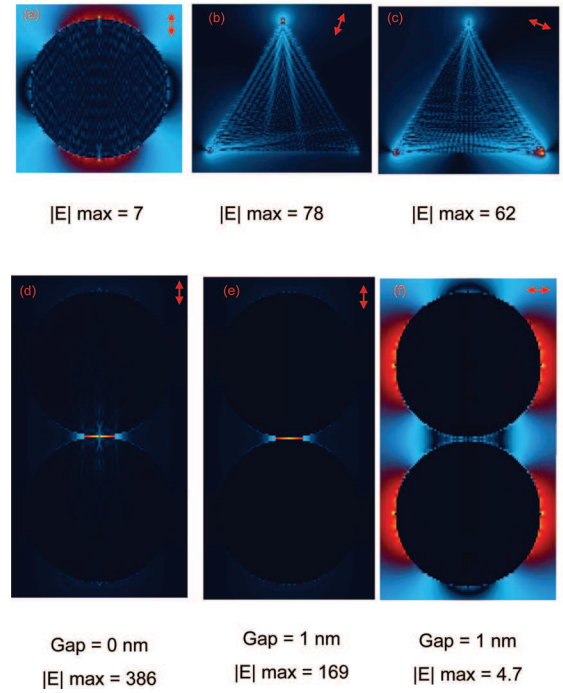

Figure 5. Electric field strength maps prepared from DDA calculations for (a) an 80 nm spherical monomer with the incident electric field vertically polarized; (b) a 119 nm altitude triangular nanoprism with incident electric field polarized at 22° from the vertical direction; (c) the same nanoprism excited with the incident electric field polarized at 112° from the vertical direction; (d) two coupled 80 nm NPs (with 0 nm gap) excited with vertically polarized electric field; (e) two coupled 80 nm NPs separated with 1 nm gap excited with incident vertically polarized electric field; and (f) two coupled 80 nm NPs separated with 1 nm gap with incident horizontally polarized electric field. All field maps were computed for the 635 nm excitation with **K**-vector propagating into the plane of the figure. Field strength was normalized to the amplitude of the incident electric field. The double headed arrow indicates the polarization direction of the incident electric field.

pointed out that with this polarization, the field in the region of the interparticle junction is depleted and shows the minimum field strength. The maximum calculated electric field strength of 4.7 is somewhat lower than that of an isolated spherical monomer.

The two trimers (VII and VIII) in Figure 4c,d have similar geometry but have orientations differing by approximately 90° from each other. As for the dimers, the LSPR response of the trimers are also broad, but the trimer LSPR also exhibited a second resonance in the near-infrared spectral region as depicted in Figure 4g,h. Particle VII is made up of three roughly equal sized spheres with diameters of 97, 104, and 103 nm while the three spheres particle VIII have slightly smaller diameters of 88, 95, and 93 nm. As the Rayleigh scattering intensity is strongly dependent on the size of the NPs, it is not surprising that the smaller trimer VIII has a weaker LSPR intensity of the two trimers (compare Figure 4g,h). SERS responses of the two trimer NP aggregates are shown in Figure 4k,l. As above, the blue traces were obtained with vertically polarized excitation radiation and the red traces with horizontally polarized light. SERS spectra of the trimers showed much smaller dependency on excitation polarization. It is instructive to extend the model of dimer SERS enhancement to trimers. When a trimer forms, three interparticle junctions are created and these are expected to be the locations of the greatest electric field strength. Since all three interparticle junctions, seen as vectors, have components parallel to both vertically and horizontally polarized excitation,

the SERS intensity is expected to appear much more isotropic than for the dimers. This is indeed the case. Although the study of both dimer and trimer cases very much resembles that of the SMSERS study, it is important to again draw the attention to the higher concentration of adsorbate used in this study. The SERS polarization anisotropy observed in the dimer response strongly suggests that contributions of the molecule outside of the "hot-sites" are very small.

Finally, we estimated the difference in the SERS intensity for a single NP versus the NP aggregates. Comparing the integrated intensity of the C≡N band of the SERS spectrum obtained from the only SERS active individual NP, the triangular nanoprism (particle IV) to the SERS intensity of the various dimers and trimers (Figure 4i−l), it is clear that the SERS intensity from the monomer is approximately 3 orders of magnitude weaker than for the dimer or trimer NP aggregates. It also worth pointing out that we did not observe any significant increase of the SERS signal from larger aggregates. All aggregates interrogated in this study showed intense SERS activity. However, the larger aggregates, such as those formed of 3−9 NPs, had lower SERS intensity than the dimers (See Supporting Information, Table 1). Even considering the complexity of the various aggregate structures and that the interparticle junctions of the larger NP are not all ideally oriented to benefit from the optimal polarization direction, nevertheless it is striking to observe that creation of more "hot-sites" for SERS in these larger aggregates actually resulted in no increase of the overall SERS intensity. Of course, it is likely that the optimal SERS enhancement for the larger NP aggregates occurs at another wavelength.

Conclusions

We have studied the light-scattering response of isolated individual NPs and small NP aggregates and have correlated these scattering spectra to high-resolution AFM images of the NP structures. Among all of the probed NPs, all aggregates, including dimers, trimers, and more complex multimers showed intense SERS activity and in the cases of dimers exhibited strong polarization anisotropy. All but one of the monomers exhibited no measurable SERS activity. The exception was a triangular nanoprism that exhibited an LSPR peaked near 600 nm and a SERS response that is approximately 3 orders of magnitude lower in the intensity than that obtained from dimer NPs. Of note, single particle SERS reported in the literature thus far were all obtained from "compound" NPs such as Au nanoshell and Au nanostar which exhibit extensive surface roughness that can act as local "hot-sites".[23,24] In addition, the LSPR of these compound particles were also tuned to match the excitation wavelengths. We have performed DDA calculations of the scattering response and prepared maps of the electric field distribution about individual NPs (monomer) and dimers to gain insights into the observed differences in SERS response. These calculations have shown that the SERS enhancement factor of a tightly coupled dimer is approximately 3 orders of magnitude greater than that of triangular nanoprism and this is consistent with the observed experimental value. Compared to a spherical NP, the nanoprism and coupled dimer exhibited SERS enhancements that are 4 and 7 orders of magnitudes larger. We have found that although we have saturated the surface of the NPs with reporter molecules, the SERS response closely resembles that of the observations in SMSERS. This study suggests that aggregation of NPs, and hence the creation of SERS "hot-sites", remains the dominant factor in enabling intense SERS activity.

Supporting Information Available: This material is available free of charge via the Internet at http://pubs.acs.org.

References and Notes

(1) Moskovits, M. *Rev. Mod. Phys.* **1985**, *57*, 42.
(2) Moskovits, M. *J. Raman Spectrosc.* **2005**, *36*, 485.
(3) Michaels, A. M.; Jiang, J.; Brus, L. *J. Phys. Chem. B* **2000**, *104*, 11965.
(4) Kneipp, K.; Wang, Y.; Kneipp, H.; Perelman, L. T.; Itzkan, I.; Dasari, R.; Feld, M. S. *Phys. Rev. Lett.* **1997**, *78*, 1667.
(5) Michaels, A. M.; Nirmal, M.; Brus, L. E. *J. Am. Chem. Soc.* **1999**, *121*, 9932.
(6) Nie, S. M.; Emery, S. R. *Science* **1997**, *275*, 1102.
(7) Xu, H. X.; Bjerneld, E. J.; Kall, M.; Borjesson, L. *Phys. Rev. Lett.* **1999**, *83*, 4357.
(8) Camden, J. P.; Dieringer, J. A.; Wang, Y. M.; Masiello, D. J.; Marks, L. D.; Schatz, G. C.; Van Duyne, R. P. *J. Am. Chem. Soc.* **2008**, *130*, 12616.
(9) Aravind, P. K.; Metiu, H. *J. Phys. Chem.* **1982**, *86*, 5076.
(10) Aravind, P. K.; Metiu, H. *Surf. Sci.* **1983**, *124*, 506.
(11) Aravind, P. K.; Nitzan, A.; Metiu, H. *Surf. Sci.* **1981**, *110*, 189.
(12) Xu, H. X.; Aizpurua, J.; Kall, M.; Apell, P. *Phys. Rev. E* **2000**, *62*, 4318.
(13) Park, W. H.; Ahn, S. H.; Kim, Z. H. *ChemPhysChem* **2008**, *9*, 2491.
(14) Sztainbuch, I. W. *J. Chem. Phys.* **2006**, 125.
(15) Kennedy, D. C.; Tay, L. L.; Lyn, R. K.; Rouleau, Y.; Hulse, J.; Pezacki, J. P. *ACS Nano* **2009**, *3*, 2329.
(16) Love, J. C.; Estroff, L. A.; Kriebel, J. K.; Nuzzo, R. G.; Whitesides, G. M. *Chem. Rev.* **2005**, *105*, 1103.
(17) McFarland, A. D.; Young, M. A.; Dieringer, J. A.; Van Duyne, R. P. *J. Phys. Chem. B* **2005**, *109*, 11279.
(18) Draine, B. T.; Flatau, P. J. *J. Opt. Soc. Am. A* **1994**, *11*, 1491.
(19) Draine, B. T.; Flatau, P. J. http://arxiv.org/abs/0809.0337, 2009.
(20) Kelly, K. L.; Coronado, E.; Zhao, L. L.; Schatz, G. C. *J. Phys. Chem. B* **2003**, *107*, 668.
(21) Jin, R. C.; Cao, Y. W.; Mirkin, C. A.; Kelly, K. L.; Schatz, G. C.; Zheng, J. G. *Science* **2001**, *294*, 1901.
(22) Jiang, J.; Bosnick, K.; Maillard, M.; Brus, L. *J. Phys. Chem. B* **2003**, *107*, 9964.
(23) Talley, C. E.; Jackson, J. B.; Oubre, C.; Grady, N. K.; Hollars, C. W.; Lane, S. M.; Huser, T. R.; Nordlander, P.; Halas, N. J. *Nano Lett.* **2005**, *5*, 1569.
(24) Hrelescu, C.; Sau, T. K.; Rogach, A. L.; Jackel, F.; Feldmann, J. *Appl. Phys. Lett.* **2009**, 94.

JP9093222